



Effect of bubble distribution on wall drag in turbulent channel flow

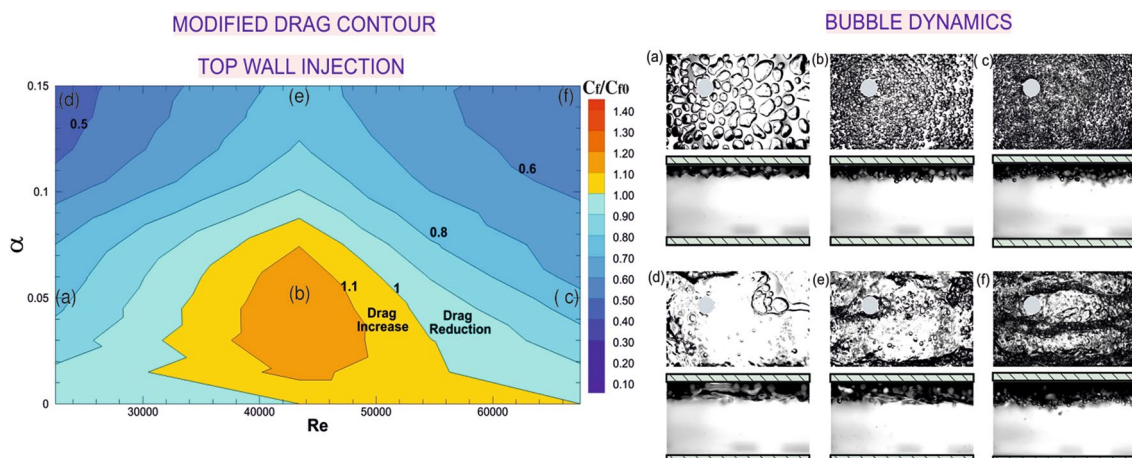
Narsing K. Jha^{1,2} · Anubhav Bhatt^{1,3} · Raghuraman N. Govardhan¹

Received: 15 March 2019 / Revised: 23 June 2019 / Accepted: 1 July 2019 / Published online: 16 July 2019
© Springer-Verlag GmbH Germany, part of Springer Nature 2019

Abstract

Skin-friction drag reduction in (water) turbulent boundary layers using bubble injection has been studied for some time. Ceccio (Annu Rev Fluid Mech 42:183–203, 2010) and Murai (Exp Fluids 55(7):1–28, 2014) have compiled drag reduction data from a number of different studies and facilities, and highlighted the large differences and scatter in the data even at the same bubble void fraction. Motivated by this, in the present work, we experimentally investigate within a single horizontal turbulent channel facility, drag modification using bubbles over a wide range of bubble void fraction ($0 < \alpha < 0.15$), channel Reynolds number ($22,500 < Re < 67,500$), and the orientation of bubble injection (top/ bottom wall). In each of the cases, we have simultaneously measured drag modification and visualized the bubble dynamics. The drag modification is obtained from measurement of the mean pressure drop at four different vertical locations within the channel. The results show that even in the same facility, the drag reduction obtained at a fixed void fraction (α) can be very different due to changes in bubble dynamics caused by changes in the other flow parameters. The visualizations show a number of bubble dynamics regimes depending on the parameters, with possibilities of both increased and decreased drag compared to the base (no bubble) case. The measurements for the bubble cases show significant vertical variations in the measured pressure drop within the channel, with these vertical variations being also dependent on the bubble distribution/dynamics. Interestingly, in some cases, the pressure drop at a given height even becomes negative, although the integrated pressure drop over the channel height, which is related to the overall drag, remains positive but lower than the base case. In terms of the overall drag, the top-wall injection is observed to give good drag reduction over a wide range of flow Re and α , but is seen to saturate beyond a threshold α . In contrast, the bottom-wall injection case shows that drag continuously decreases with α at high channel Re , while at low channel Re , the drag is found to continually increase with α . The present study shows a maximum of about 60% increase and a similar 60% reduction in wall drag over the entire range of conditions investigated. For each of the bubble wall injection orientations (bottom/top/both wall), contour plots of drag modification and gain factor (fractional drag reduction per unit void fraction) are presented in the plane of α and Re along with the corresponding bubble dynamics, which helps to delineate the different regimes seen in such bubbly channel flows.

Graphic abstract



Extended author information available on the last page of the article

1 Introduction

Skin-frictional drag is a major component of resistance in transportation systems like ships, and hence, there has been a lot of interest in reducing it to save fuel. Injection of bubbles in the (water) boundary layer of ships is one of the possible ways of reducing skin-frictional drag in turbulent boundary layers, and it has long been a focus for researchers with the expectation that it can be applied to ships and liquid pipelines. Addition of surfactant and polymers, and use of super-hydrophobic surfaces are other possible ways to reduce drag of turbulent boundary layers (Ceccio 2010; Rothstein 2010; White and Mungal 2008).

The use of bubbles as a way of reducing skin-frictional drag in turbulent flows had started with the initial pioneering work by McCormick and Bhattacharyya (1973). They showed, followed by many other studies (Madavan et al. 1985; Guin et al. 1996; Sanders et al. 2006; Elbing et al. 2008), that the drag reduction using bubbles is highly dependent on the bubble void fraction and its distribution very close to the wall as most of the turbulent transport responsible for the production of wall drag takes place within the few tens of wall units near the surface (Pope 2000). There are a few broad mechanisms that are known to affect wall drag in bubbly turbulent boundary layers. First, there is the modification of fluid properties like density and viscosity of the bubbly flow (L'vov et al. 2005). Second, there is the effect of compressibility and deformation of the bubble on the flow (Lo et al. 2006; Van Gils et al. 2013). Third, the bubble will interact with the turbulent flow and may affect the turbulent transport either by lifting the structure away from the wall and thus affecting the production (Ferrante and Elghobashi 2004), or by suppressing the vortical structure (Lu et al. 2005; Sridhar and Katz 1999; Jacob et al. 2010; Jha and Govardhan 2015). Fourth, there can be bubble–bubble interactions and bubble splitting affecting the eddy distribution and properties (Meng and Uhlman 1998).

Besides the above four reasons, there is also the possibility of the formation of an air layer close to the wall changing the boundary layer dynamics near the wall (Elbing et al. 2008). Different kinds of bubble dynamics, bubble size distribution, and coalescence time scale will result in different physical mechanisms being responsible for drag reduction (Murai 2014). A parameter that is useful to measure the effectiveness of bubble-induced drag reduction for different physical mechanisms is the “Gain factor” defined as the fractional drag reduction per unit void fraction (Murai 2014). Gain factor is naturally a function of the physical mechanism responsible for drag reduction. It is important to note here that the effect of bubbles on drag is a function of bubble size and flow speed, and depending on these parameters, one can have drag reduction, increase, or no

change at all (Murai 2014). Murai (2014) in his review summarizes the work of a number of studies on bubble injection in a horizontal channel. These studies generally report on injection from the top wall of the channel, where buoyancy helps to keep the injected air close to the top surface for sustained drag reduction. He also discusses the different bubble dynamics regimes and possible physical mechanisms for drag reduction.

Sanders et al. (2006) and Elbing et al. (2008) have studied drag reduction at very high Reynolds numbers on a flat plate in a large-scale facility due to its possibility of being used for drag reduction in ships and other underwater vehicles. Besides these studies, a large amount of work have been done to study the feasibility of this technique for drag reduction of ships (Latorre et al. 2003; Kumagai et al. 2015; Mizokami et al. 2010), and they have observed about 10% drag reduction. Van Gils et al. (2013) and Verschoof et al. (2016) have shown experimentally in a turbulent Taylor–Couette flow that bubble deformability is a crucial and important mechanism for drag reduction. A study on bubble injection from the lower wall of a channel was done by Gabillet et al. (2002), where the bubbles naturally migrate away from the wall, with the study reporting on measurements of both the water velocity and measurements of the void fraction and bubble diameter.

Despite these experimental and numerical studies, there are many unanswered questions as stated in the review of Ceccio (2010). He has compiled drag reduction data for turbulent boundary layers, both from zero-pressure gradient flat plate and channel flows, and has shown large variations in drag reduction for the same bubble void fraction among different experiments. This points both to the lack in complete understanding of the physical mechanisms of drag reduction using bubbles, and to the fact that there is scatter between the many different facilities from which such data have been compiled. In this connection, it should be noted that measurements of modified drag over a wide parameter space coupled with bubble dynamics from a single facility do not exist in the literature. In the present study, we thus explore, in a single horizontal turbulent channel facility, a wide range of parametric space including flow Reynolds number, bubble void fraction, and orientation of injection (top/ bottom wall) to help address the observed scatter in the reviews of Ceccio (2010) and Murai (2014). At each of the different conditions, we simultaneously measure the mean pressure drop at different vertical locations within the horizontal channel to obtain modified drag, and visualize the bubble dynamics in two perpendicular planes. A schematic of the experimental arrangement used in the present study is shown in Fig. 1, indicating that a large number of bubbles are injected into a fully developed horizontal turbulent channel flow either from the top or bottom wall at different injection rates and channel Re . Using the modified drag data and

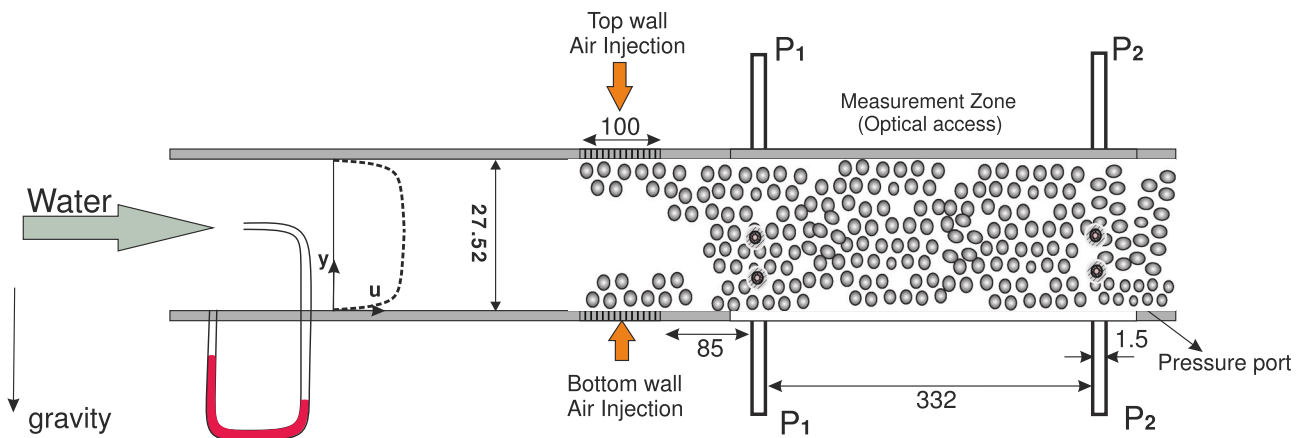


Fig. 1 Schematic showing the main components of the experimental set-up used for injection of bubbles into a fully developed horizontal channel test section. The air injection ports on both top and bottom walls, the transparent section for bubble visualization, and pressure ports are shown along with the important dimensions. Pressure ports

for pressure drop measurements are located at four vertical locations inside the channel; two in the mid-plane corresponding to the top and bottom walls, and another two on the side walls at quarter and central height from the bottom wall. All dimensions shown are in mm

the simultaneous bubble dynamics from a single facility, we create, in the present work, a drag modification regime map in the plane of void fraction and channel Reynolds number for both top- and bottom-wall injection conditions.

This paper is laid out in the following manner. In the next section (Sect. 2), we shall describe the experimental set-up used for the present study and velocity measurements within the channel without bubbles for validation of the turbulent channel flow set-up. The experimental techniques used for pressure drop measurement, bubble visualization, and velocity field measurements are also discussed here. Subsequently, experimental results are presented in Sect. 3 for bubble dynamics and pressure drop measurement. This section is further divided into sub-sections for bottom- and top-wall injection. Finally, the conclusions are presented in Sect. 4.

2 Experimental methodology

For the present work, a fully developed horizontal large aspect ratio turbulent channel flow set-up with water as the fluid medium was developed. The channel aspect ratio (span/height) was about 12, which is large enough to ensure a nearly two-dimensional flow in the mean sense (Monty 2005). A schematic of the test section with measuring instrumentation is shown in Fig. 1. The test section is 871 mm long, 304.8 mm wide, and has a height of 27.5 mm. At the time of final assembly, the channel height was measured at several stream-wise and span-wise locations, and variations were seen to be within 1.5%. Mean flow speed (u_m) in our experiments is in the range of 0.67–2.01 m/s, which corresponds to channel Reynolds number ($Re = u_m H / \nu$) of

22,500–67,500, where u_m , H and ν are mean velocity, full channel height, and kinematic viscosity of water, respectively. The value of ν is $0.818 \times 10^{-6} \text{ m}^2/\text{s}$ at laboratory condition. Experiments were done at four channel Re of 22,500, 43,400, 54,600, and 67,500.

2.1 Experimental set-up

A large water tank with capacity of 2000 l was used for storage of water and purging of air. Water from the tank was pumped to the test section using a centrifugal pump with maximum flow rate of 23 l/s and 6–15 m water head. Flow rate of the pump was controlled by controlling the RPM of the AC motor using a frequency controller from Integrated Electric Co. Pvt. Ltd. (ISAC05M, 3 phase, 6 KVA). Pump discharge was connected to the channel main line through a flexible rubber coupling that acted as a vibration damper, minimizing the vibrations conveyed to the channel from the pump. The working fluid (water) from the pump entered the diffuser, whose diffusing angle was kept small to minimize chances of flow separation. Water then reached the 300 mm-long settling chamber through the impacter plate. The settling chamber had a rectangular cross-section packed with 5 mm-diameter and 300 mm-long plastic straws, which was followed by a 418 mm-long convergent section. The converging section was connected to a 2 m-long development channel, which was long enough to allow the flow to become fully developed by the time which it enters the test section, as will be shown later in the next sub-section. The test section was made with a stainless-steel framework with transparent perspex observation windows on the top, bottom, and the two sides. After the test section, water flowed into a 543 mm-long divergent section, which was then connected

through a pipe that discharged the water into the storage tank, from where water was drawn by the pump. To remove residual air from the channel during the initial engagement of the pump and prevent stray air pockets, three purge lines were provided at higher locations of the channel. A schematic of the experimental arrangement is shown in Fig. 1. A Pitot tube was connected upstream of the bubble injection location to monitor and maintain constant center-line velocity/flow rate as compared to the no-bubble case. Bubbles were injected either from top or bottom or both walls through a 100 mm porous plate section. The porous plate had a mean pore size of about 10 μm with 33% porosity and a thickness of 10 mm. The sintered porous plate was pressurized through an air chamber with bubble formation taking place at the porous surface in contact with the water in the channel. Flow rate of air was controlled with an Alicat Scientific (MCR 1000 slpm) mass flow controller with an accuracy of about $\pm 1\%$. The bubble diameter near the porous plate varied from 200 to 400 μm depending on the conditions. The transparent window for visualizing the bubble dynamics started 85 mm after the end of the bubble injection section. The pressure drop measurements were done a little downstream (85 mm) of the porous plate over a stream-wise length of 332 mm, this pressure drop measurement being done at four vertical locations, as will be discussed later. The bubble dynamics were imaged from both the top- and side-views using two high-speed Phantom Miro-M110 cameras, with the stream-wise length of visualization corresponding to 144 mm for the top-view, and 65 mm for the side-view visualization, the difference in field of view being related to the larger size of the bubble structures in the top-view. These are the main bubble visualizations presented in this work. Uniform background illumination for this was obtained from a 1000 W halogen lamp in conjunction with a diffuser sheet. Given the distance between pressure ports of 332 mm, the top- and side-view visualizations shown throughout this work correspond to the initial 43% and 20% of the distance between the pressure ports. In addition, a downstream camera was used for side-view visualization between 80 and 100% of the distance between pressure ports, to get a sense of the bubble distribution towards the end. The side-view images showed the vertical location of the bubbles within the channel, and these were used with some image analysis to obtain quantitative estimates for the vertical location of the bubbles within the channel for bottom-wall injection case, and for measuring the air/bubble layer thickness for the top-wall injection case, as discussed in Sect. 3.

2.2 Characterization of fully developed horizontal turbulent channel flow

Velocity fields were obtained within the channel for the base case (without bubbles) from time-resolved particle image

velocimetry (PIV) measurements for validation of the base turbulent channel flow. For this purpose, the flow was seeded with silver-coated hollow glass spheres with a mean diameter of 14 microns. The seed particles were illuminated by a laser sheet from a high repetition double-pulsed LDY-301 Litron PIV laser with a maximum energy of 10 mJ/pulse. The images were then processed with Dantec PIV software using adaptive correlation with three-step box size refinement with the final box size being 32×32 pixels or 16×16 pixels. Correlation box overlap was maintained at 50% in all cases, with each box having roughly at least 6–8 particles to ensure strong correlations similar to Jha and Govardhan (2015). For the mean velocity field, the average of 2000 instantaneous flow fields was taken. The mean stream-wise velocity (u) profile in Fig. 2a is normalized by the center-line velocity (u_c) and is plotted against the vertical distance (y) normalized by the half-channel height ($H/2$). For comparison and validation, the data from Wei (1987) for a two-dimensional fully developed turbulent plane-channel flow are also shown in the figure, with reasonable agreement between their data at Re of 39,582 and ours at Re of 22,500 and 67,500. Figure 2b shows the mean stream-wise velocity profile in the traditional log-law form above the buffer region. For log law of the wall, von Kármán constant and additive constant are 0.4 and 3.5, respectively, which is very similar to the high-resolution data of Zanoun et al. (2003). Friction velocity (u_τ) calculated from the velocity field is found to be 0.097 m/s for Re of 67,500. After about 400 wall units, in the wake region, deviation of the data from the log law may be seen till the center of the channel, which is due to the large-eddy structures in the flow (Coles 1956).

Pressure drop measurements were done for the fully developed turbulent channel without bubbles to validate the base case flow field, and then, wall drag was calculated from the measured pressure drop by force balance on a control volume. The pressure drop was measured using a Ashcroft pressure sensor (GC52; Wet/Wet Differential Pressure) having response time of 100 ms and a range of 0–4 inches of water column. The pressure drop was measured between two stream-wise locations separated by a stream-wise distance of 332 mm or 12 channel heights (H). This measured pressure drop and the drag values obtained from it are an average value over the stream-wise length between the two pressure ports. We have chosen a long stream-wise distance of about 12 channel heights ($12H$) between pressure ports to get the integrated drag over this length, which would be a quantity of interest for overall pressure drop/drag of the channel. Pressure drop was measured at different vertical locations across the channel height, as it was found to vary significantly with vertical location because of the asymmetric distribution of bubbles with height inside the channel. During experiments with bubble injection, some air was occasionally trapped in the transparent piping of the pressure measurement line and care was taken to purge these

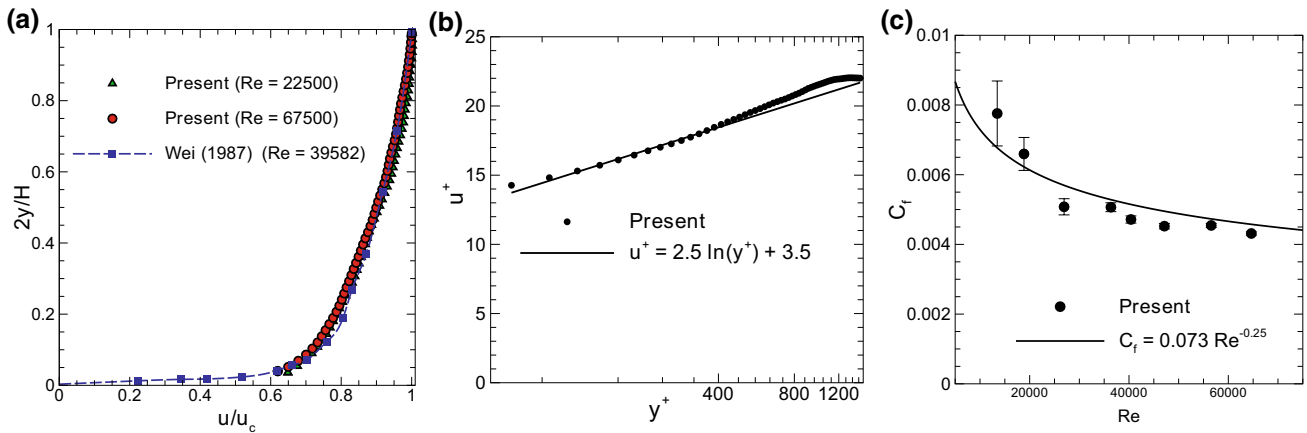


Fig. 2 Comparison of the velocity profile and wall shear stress from the present experiments for the no-bubble case with data from literature. **a** Mean stream-wise velocity (u) profile across the half-channel height measured using PIV. Present measurements at two channel Reynolds numbers are compared with the measurements of Wei (1987) at $Re = 39,582$. In the figure, the stream-wise velocity is nor-

malized by the center-line velocity (u_c), while the vertical distance is normalized by the half-channel height ($H/2$). **b** Stream-wise mean velocity profile in the traditional log-law form for flow Re of 67,500 at bottom wall of the channel. Von Kármán and additive constant is also shown in the plot. **c** Skin-friction coefficient (C_f) as a function of Re plotted along with the empirical correlation of Dean (1978)

lines to remove such trapped air bubbles before continuing with measurements. The calculated wall drag from pressure drop measurements was used to obtain the skin-friction coefficient (C_f) and its variation with flow Re is plotted in Fig. 2c along with the well-established empirical relation given by Dean (1978). Experimental uncertainty using a Gaussian propagation method for C_f is also plotted to get an estimate of confidence in the measured skin-friction coefficient. From the plot, it may be seen that the present measurements are in reasonable agreement with the established correlation giving confidence in the adopted methodology.

3 Results

We report here the results from our studies on bubble injection in to a fully developed horizontal channel including both drag measurements and bubble visualization. As stated earlier, the focus of the work is to investigate in a single horizontal turbulent channel facility, a wide range of parametric space including flow Reynolds number, bubble void fraction, and orientation of injection (top wall/bottom wall) to help address the observed scatter in the reviews of Cecio (2010) and Murai (2014). The bubble void fraction (α), which is the ratio of the volumetric flow rate of injected air (Q_a) to that of the total flow rate in the channel ($Q_w + Q_a$), is varied from 0 to about 0.175 (Q_w is the water flow rate through the channel). This void fraction is controlled by an air-flow controller feeding air to the bubble injection system. Experiments are done at seven bubble void fraction (α) of 0.025, 0.05, 0.075, 0.1, 0.125, 0.15, and 0.175. The experimental arrangement permits injection of bubbles through

porous plates from only the top wall, or only the bottom wall, or from both the walls. We have studied and report results on all these three combinations, with the main focus being on the only bottom or only top-wall injection cases. In addition, the channel Reynolds number has been varied over the range from about 22,500 to about 67,500 at four Reynolds numbers ($Re = u_m H/\nu$) of 22,500, 43,400, 54,600, and 67,500, where u_m is the average velocity across the height of the channel. From these systematic measurements over a range of parameters, we attempt to identify different bubble dynamics regimes and relate it to the vertical pressure drop distributions and wall drag within the channel.

As discussed in the introduction, bubbles can reduce the drag of turbulent boundary layers either due to modification of fluid properties or due to its interaction with turbulence. Drag reduction due to modification of fluid properties such as water density and velocity are relatively simple effects and not difficult to explain. To focus our attention on drag reduction from the more interesting and complex turbulence–bubble interaction, we normalize the wall drag using the modified density and velocity to remove any variations (reductions) caused by changes in fluid properties. For the normalization of the wall shear stress in the presence of bubbles, to obtain the skin-friction coefficient (C_f), we thus use the modified density and velocity as discussed below.

The primary assumption for getting the modified water properties in the presence of bubbles is that the bubbles (or air) are uniformly distributed in the water. It is then simple to obtain a relation for the effective density of the bubbly water (ρ_{eff}) in terms of the water density (ρ_w) as given by the following:

$$\rho_{eff} = \rho_w(1 - \alpha). \tag{1}$$

The effective velocity of the bubbly mixture is higher due to the additional volumetric flow rate of injected air. This can be accounted for by a new effective mean velocity (u_{eff}), which can be obtained from volume conservation assuming that both air and water are incompressible, as given by the following:

$$u_{\text{eff}} = (Q_a + Q_w)/A = u_m/(1 - \alpha), \quad (2)$$

where u_m is the mean (water) velocity in the channel upstream of bubble injection and A is the cross-sectional area of the channel.

For the non-dimensionalization of wall shear stress (τ_w), to find the skin-friction coefficient (C_f), we now use the effective flow velocity (u_{eff}) and fluid density (ρ_{eff}) as defined above along the lines of Oishi et al. (2009). We refer to the skin-friction coefficient for the base case in the absence of bubbles as C_{f0} . The ratio of the skin-friction coefficient with bubbles to that of the base case is thus as follows:

$$\frac{C_f}{C_{f0}} = \frac{\tau_w/(0.5\rho_{\text{eff}}u_{\text{eff}}^2)}{\tau_{w0}/(0.5\rho_w u_m^2)} = \frac{\tau_w(1 - \alpha)}{\tau_{w0}}. \quad (3)$$

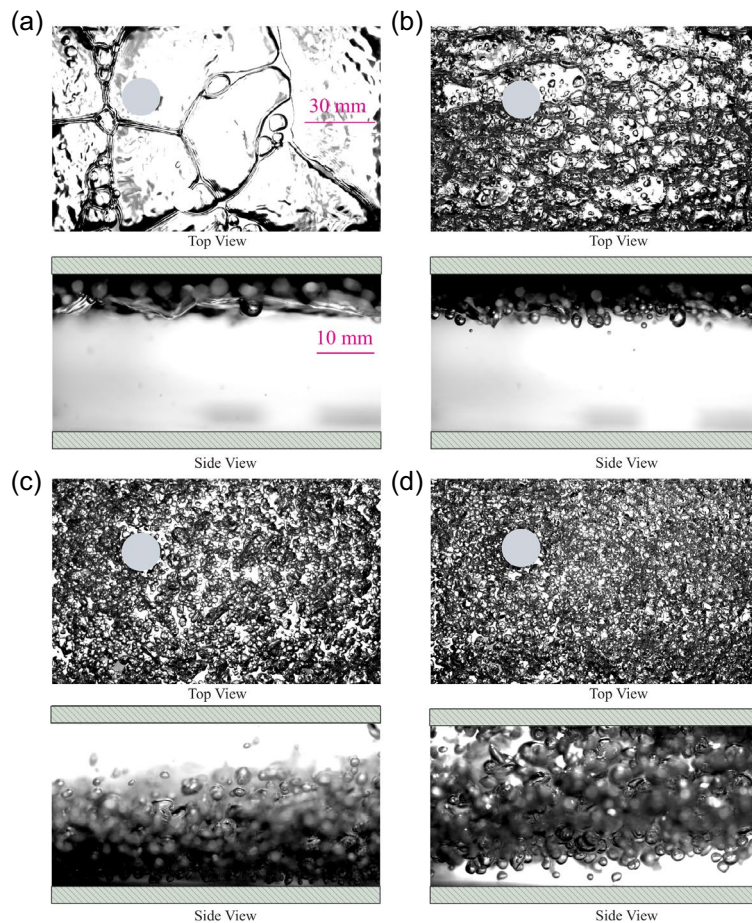
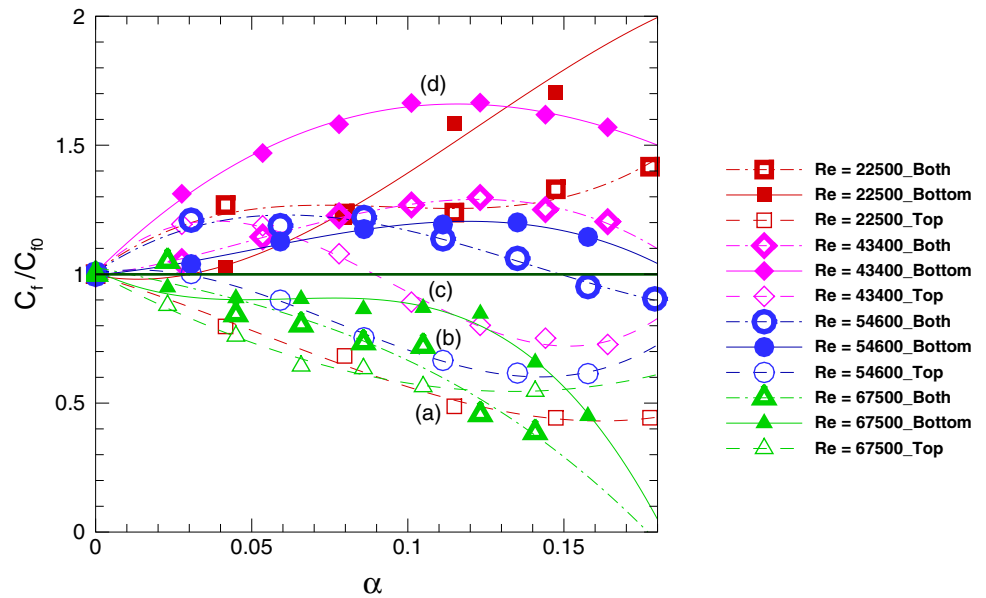
We begin by plotting drag reduction/modification data (C_f/C_{f0}) from our experiments done in a single facility, in a manner similar to that done by Ceccio (2010) for data from many different facilities and studies. The resulting plot shown in Fig. 3 includes our (C_f/C_{f0}) data for all cases investigated in this study, including variations in Re , α , and injection orientation (top/bottom wall), plotted versus the corresponding void fraction (α). One obvious observation is that there is still large scatter in C_f/C_{f0} values even at the same α , although all experiments shown here have now been done in a single facility. This scatter of data can now be purely attributed to the different bubble dynamics regimes as all other extraneous issues resulting from different facilities/experimental artifacts have been removed, as they are now done in a single facility.

A closer look at one void fraction (α) value, say about 0.1, in Fig. 3, shows that C_f/C_{f0} values vary considerably from 0.5 to 1.6, which corresponds to 50% drag reduction to 60% drag enhancement. The lowest C_f/C_{f0} value of 0.5 (marked as Fig. 3a) is seen to correspond to top-wall injection at Re of 22,500, and the corresponding bubble dynamics is shown in Fig. 3a. We can see from the bubble dynamics (shown in two perpendicular planes) that all the injected bubbles have formed an air layer on the top wall (see top-view) and K–H waves can be seen on the air layer (see side-view). This kind of an air layer effectively reduces the shear stress at the wall because of the lower viscosity of the air layer. At a slightly higher C_f/C_{f0} of about 0.68 (marked as Fig. 3b), the Reynolds number is also higher than in Fig. 3a ($Re = 54,600$), linked to the change in bubble dynamics from an air layer

to more discrete bubbles near the top wall (see Fig. 3b) that are much smaller than the very large flat air bubbles/layer seen in Fig. 3a. The discrete bubbles in Fig. 3b are, however, still of reasonable size with relatively smaller bubbles away from the wall, and some bubble waves may also be seen in this case. This points to the fact that a clear air layer is more efficient at reducing drag than the large number of discrete bubbles seen in Fig. 3b. At even higher C_f/C_{f0} of about 0.88 (marked as Fig. 3c), the injection method corresponds to bottom-wall injection at a Re of 67,500. In this case, there are no bubbles at the top wall, and the bubbles are seen close to the lower wall and in the center of the channel (see Fig. 3c). The bubbles close to the lower wall are likely helping in suppressing the intense turbulence near the lower wall, which results in a small about 10% reduction in drag. At the largest C_f/C_{f0} of about 1.6 (marked as Fig. 3d) corresponding to bottom wall injection and a lower Re of 43,400, the bubbles have risen from the lower wall, and are seen between the center of the channel and the top wall. The size of the coalesced bubbles is seen to be relatively larger here ($D_b \sim 2$ mm) with the likelihood of strong shedding behind the bubble and increased turbulence leading to the large enhancement of drag by about 60%. To get a sense of the relative velocities of bubble with respect to the flow, and help determine the relative Reynolds numbers for a bubble in turbulent channel flow, we have used bubble tracking and two-phase time-resolved PIV to get both the bubble velocity and the fluid velocity around single bubble injected into the channel. This was done by injection of single bubbles of diameter 0.3 mm, 1 mm, and 1.5 mm at channel flow Re of 67,500. The measured relative bubble velocity for 0.3 mm, 1 mm, and 1.5 mm were 0.136, 0.05, and 0.24 m/s, respectively. The bubble Reynolds number based on relative velocity of bubble with respect to the flow and bubble diameter is 50, 60, and 440 for bubble diameter of 0.3 mm, 1 mm, and 1.5 mm, respectively. It is clear from these measurements that bubbles with size greater than 1.5 mm would have crossed critical Re for shedding. This indicates that for case Fig. 3d discussed above with bubble diameter of 2 mm, strong shedding would be expected with consequent drag increase.

One interesting point to note in the drag plot of Fig. 3 is the crossing of the trend lines for bottom-wall injection at Re of 67,500 (solid green line) and for top-wall injection at Re of 43,400 (dashed pink line) at $\alpha = 0.1$. The bubble visualization images for these two cases are shown in Fig. 4. Here, Fig. 4a, c shows side- and top-views for bottom-wall injection at Re of 67,500, while Fig. 4b, d shows side- and top-views for top-wall injection for Re of 43,400. It can be seen here that there are differences in vertical spread, size, and distribution of bubbles in the two cases, although the modified drag is nearly the same in both cases. This highlights

Fig. 3 Variation of non-dimensional skin-friction coefficient C_f/C_{f0} with α is plotted for all 84 cases investigated in the present study. One obvious observation is the large scatter in C_f/C_{f0} values seen at the same α due to the different bubble dynamics regimes. Bubble dynamics for four different wall drag cases at α of 0.1 as indicated on the C_f/C_{f0} - α plot is also shown. The conditions corresponding to these four cases are (type of injection, Re). **a** Top 22,500, **b** top 54,600, **c** bottom 67,500, and **d** bottom 43,400. Flow is from left to right for all the bubble images

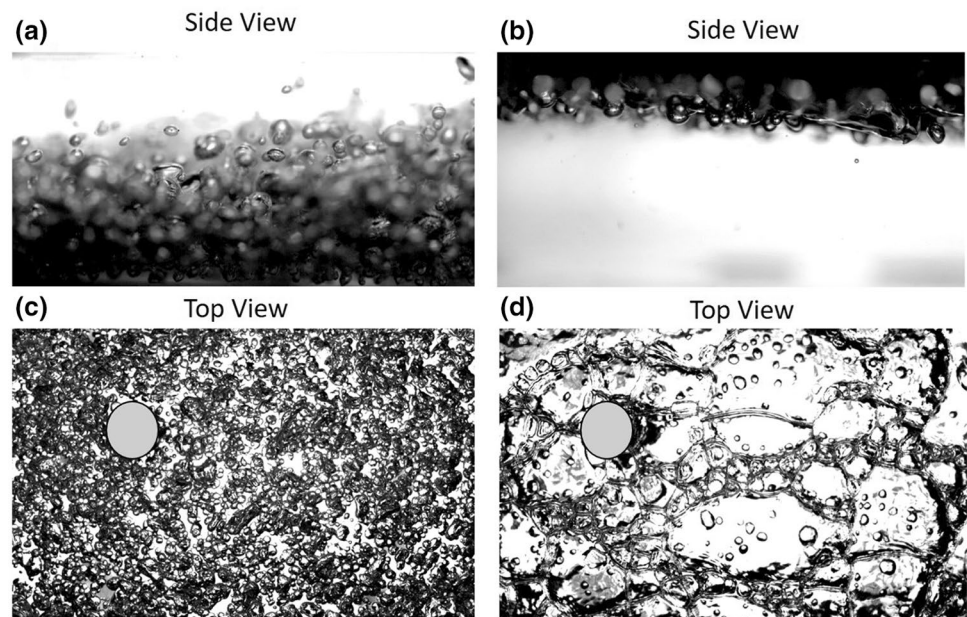


the fact that similar drag reduction does not guarantee the same bubble dynamics, although it is a fact that changes in bubble dynamics in general do affect drag.

The above results clearly indicate that wall drag is affected by changes in bubble size, shape, and relative

position of bubbles with respect to wall, even for the same void fraction. Furthermore, it is clear that the bubbles are not uniformly distributed in the vertical direction as seen in the visualizations, and this is expected to result in significant differences in pressure drop measured at different channel

Fig. 4 Plot shows the bubble dynamics for α of 0.1; **a, c** side- and top-views for bottom-wall injection at Re of 67,500. **b, d** Side- and top-views for top-wall injection at Re of 43,400. Similar drag reduction values seen in Fig. 3 does not imply similar bubble distribution. Beside the difference in vertical spread, size and distribution vary greatly



heights. We shall discuss this point in more detail as we present the pressure drop data with height for different bubble injection conditions.

We shall now systematically present drag modification data for bottom-wall and top-wall injection in two separate sub-sections. In each case, we shall present vertical variations in pressure drop within the channel, the overall modified drag for the channel, and some bubble visualizations to show the different types of bubble dynamics possible and its effects on the wall drag.

3.1 Bottom-wall injection

We shall begin by presenting the measured variation of pressure drop (ΔP) with vertical height (y) for different bubble void fraction (α) for bottom-wall injection, as shown in Fig. 5. The pressure drop (ΔP) is non-dimensionalised here by the pressure drop in the absence of bubbles (ΔP_0), noting that the mean water velocity upstream of bubble injection was maintained to be the same in both cases. It may also be noted here that the pressure ports at intermediate vertical heights were taken from the side wall to avoid any intrusion into the flow. In Fig. 5, $\Delta P/\Delta P_0$ is presented for flow Re of 22,500, 43,400, 54,600, and 67,500 in Fig. 5a–d, respectively, with different symbols used to represent different values of the void fraction (α). The most striking feature of all the plots is that substantial variations in pressure drop can be seen with the normalized vertical location y/H in all cases where there is bubble injection, i.e., non-zero void fractions. These pressure drop variations with height give spatial information about the effect of bubbles on the flow field. For example, in Fig. 5d, at $Re = 67,500$, there is substantial

pressure drop reduction at the bottom wall ($y/H = 0$), and reduction in pressure drop even at the top-wall ($y/H = 1$), but there is an increase in pressure drop along the center line of the channel, this broadly being the trend for all non-zero void fractions at this Re .

From the pressure drop at different vertical locations, as shown in Fig. 5, we can obtain the mean wall shear stress from a simple control volume (CV) analysis over the pressure drop measurement region. From horizontal momentum conservation applied to the CV, the stream-wise integral of the shear force on both the top ($\tau_{w/top}$) and bottom ($\tau_{w/bottom}$) walls will be balanced by the integrated pressure force acting on the CV and the momentum deficit as given by the following:

$$\int_0^H P_{i/l} w dy - \int_0^H P_{o/l} w dy + \int_0^H \rho u_{i/l}^2 w dy - \int_0^H \rho u_{o/l}^2 w dy = \int_0^L (\tau_{w/top} + \tau_{w/bottom}) w dl. \quad (4)$$

where $P_{i/l}$ represents the pressure at the CV inlet, and $P_{o/l}$ represents the pressure at the CV outlet, both along a vertical line, and w is the span-wise width of the channel. Given the large stream-wise extent of the CV ($L = 12H$), we have assumed that relative change in the momentum flux entering and leaving the CV to be small compared to the pressure difference force. Furthermore, the horizontal integral of the shear across both the top ($\tau_{w/top}$) and bottom walls ($\tau_{w/bottom}$) may be represented by a mean shear averaged over the stream-wise length of $L = 12H$. This would require the mean shear force over the stream-wise length to be balanced

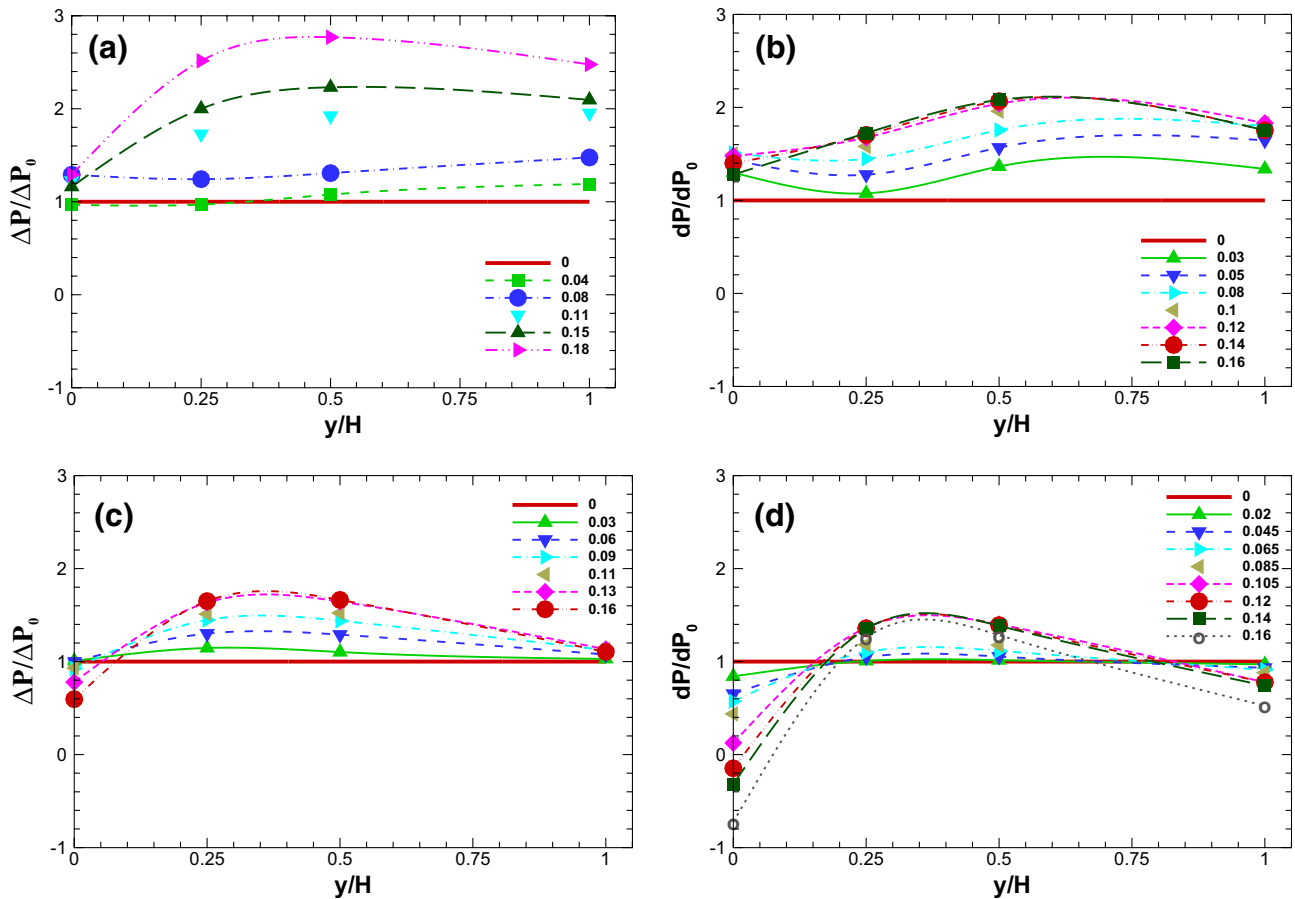


Fig. 5 Vertical variation of pressure drop non-dimensionalised by the base case pressure drop ($\Delta P/\Delta P_0$), for different void fraction (α) for bottom-wall injection. The flow Re corresponding to each of the plots is **a** 22,500, **b** 43,400, **c** 54,600, and **d** 67,500, respectively

by the pressure force and thus permits a link between vertical integral of pressure drop and the mean shear across both the top and bottom walls as given by the following:

$$(2\tau_w)L = \int_0^H (\Delta P dy). \tag{5}$$

It should, however, be noted that the above expression does have errors associated with the assumption of the momentum change being small, and the fact that the flow may not be in equilibrium state due to internal bubble events. With a view to minimize these errors, we have chosen a long stream-wise distance ($12H$) for pressure drop measurement. It should also be noted that here we only study time averaged ΔP , but there will be pressure fluctuations that can be measured with high temporal resolution sensor. This mean wall shear stress is non-dimensionalised, as discussed earlier, to obtain the skin-friction coefficient (C_f), and its ratio with the skin-friction coefficient for the no-bubble case (C_{f0}) calculated at each Re and α . A contour plot of the resulting (C_f/C_{f0}) values is shown in Fig. 7 in the $Re-\alpha$ plane. Another

parameter plotted in the same $Re-\alpha$ plane, and also shown in the figure, is the gain factor, $G \equiv \frac{1}{\alpha} \left(\frac{\tau_{w0} - \tau_w}{\tau_{w0}} \right) = \frac{1}{\alpha} \left(1 - \frac{C_f}{C_{f0}(1-\alpha)} \right)$ (using Eq. 3), which is defined as the ratio of drag reduction to the base drag for unit bubble void fraction (Murai 2014).

This gain factor is useful for measuring the effectiveness of bubble-induced drag reduction, with large positive values of G , indicating that considerable drag reduction is achieved with small amounts of air injection (α), while negative values of G indicate drag increase. The striking aspect of Fig. 7 is that there is clear organization of the modified drag data (and gain factor) when plotted in this $Re-\alpha$ plane, in contrast to the apparent scatter seen earlier in Fig. 3. Also shown in the figure are bubble visualization images at six different conditions (Fig. 7a–f), which are marked on the skin-friction plot to enable connections to be made between drag reduction or increase and the bubble dynamics. It may be noted that in the bottom-wall injection case, there is vertical motion of the bubbles due to buoyancy as seen in the side-view bubble visualization images, whose stream-wise length

corresponds to about 20% of the distance between the two pressure ports. Hence, the skin-friction values shown must be interpreted as the average value over the total distance between the two pressure ports, with the vertical travel of the bubbles in this spatially developing flow being part of this.

The vertical extent of the bubbles is apparent at any given stream-wise location from the side-view visualizations. From such instantaneous visualizations, the average bubble intensity as a function of wall-normal distance (y/H) may be obtained from averaging of a large number (about 500) of such visualizations. The average bubble intensity after removal of background and normalization could be used as a measure of the number of bubbles. This is plotted in Fig. 6 versus the wall-normal distance (y/H) for four different Re at a stream-wise location corresponding to 20% of the distance between the two pressure ports in Fig. 6a, and at a downstream location corresponding to about 80% of the distance between pressure in Fig. 6b. In these plots, average bubble intensity of zero implies that the intensity is the same as the background and may be interpreted as no bubbles, while a value of 1 corresponds to the maximum intensity of bubbles. At a given Re , comparison across the two stream-wise locations shows the vertical rise of the bubbles with downstream distance over the stream-wise length corresponding to the pressure drop measurement, with the effect being more pronounced at lower speeds or Re . An obvious reason for these is the increased time available for vertical migration due to the relatively lower flow velocity, with this also providing increased time for coalescence resulting in larger bubbles.

The other reason is that the bubble detachment diameter is larger at lower flow velocity and the lower levels of turbulence near the porous plate. These reasons together give rise to more rapid vertical migration of the bubbles at lower Re . For these same reasons, we can see that in both cases with increase in Re , the region with bubbles shifts more towards the bottom wall from where the bubbles are injected.

Apart from the location of the bubbles in the vertical direction, the other important factor influencing the drag is the average size of the bubbles and the corresponding Weber and Froude numbers, as pointed out by Murai (2014). While no intrusive measurements of the actual air distribution as a function of wall-normal distance within the channel were made during the present experiments, an average size of bubbles within the channel was obtained directly from the side-view visualizations. The average bubble size measured for the different Re and α conditions for the bottom-wall injection cases is summarized in Table 1 along with the calculated values of Weber and Froude number, the corresponding drag values, and a rough classification of the bubble dynamics regime (BDR). As in Murai (2014), the Weber number is defined here as $We = (\rho(\frac{du}{dy})^2 D_b^2) / (\sigma / D_b)$ as the ratio of shear at the bubble to the Laplace pressure inside the bubble, with $\mu \frac{du}{dy} = \tau_w = \rho u_\tau^2$. A quick look at We values in Table 1 indicate very large numbers ranging from 6000 and higher. An immediate question that arises here is if such bubbles would not be broken down by the shear present, with Murai (2014) suggesting an upper We threshold of 10

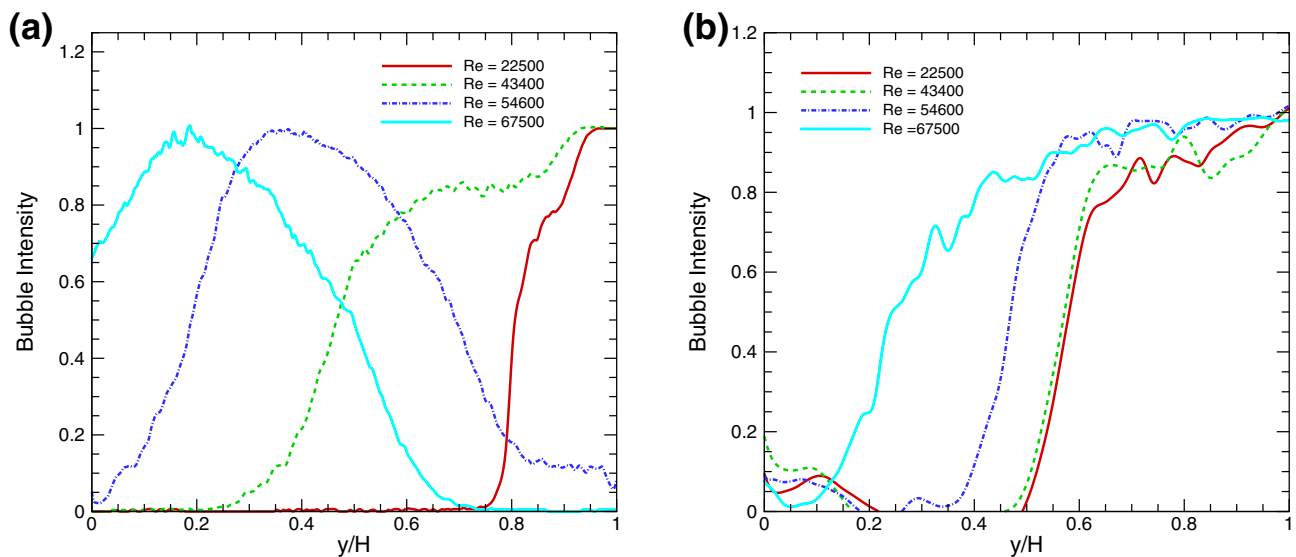


Fig. 6 Average bubble intensity as a function of the wall-normal distance (y/H) for bottom-wall injection at α of 0.05 at **a** 20% and **b** 80% stream-wise distance between the two pressure ports. This average bubble intensity is extracted from an ensemble average of 500 side-view bubble visualizations. We can clearly see in **a** that as Re is

increased, the bubble distribution shifts more towards the bottom wall which is the injection plane, while a comparison between **a** and **b** at the same Re shows the upward motion of the bubbles with stream-wise distance

Table 1 Experimental conditions, bubble dynamics regimes (BDR), bubble size, drag reduction, Froude number (Fr), Weber number (We), and bubble concentration range (BCR) for bottom-wall injection cases are summarized

Case	Re	α	BDR	D_b (mm)	C_f/C_{f0}	Fr	We	BCR (y/H)
1	22,500	0.05	Coalesced bubbles	7.3	1.05	–	–	0.78–1
2	22,500	0.1	Layering	10.9	1.44	–	–	0.67–1
3	22,500	0.15	Layering	15.9	1.71	–	–	0.63–1
4	43,400	0.05	Discrete, not in LWB	2.5	1.45	52.7	6154	0.46–1
5	43,400	0.1	Discrete, in outer log layer	2	1.65	65.9	3151	0.23–1
6	43,400	0.15	Discrete, in inner log layer	2.4	1.6	54.9	5445	0.18–1
7	54,600	0.05	Discrete, in log layer	2.2	1.09	75.4	9514	0.24–0.75
8	54,600	0.1	Discrete, in log layer	2.2	1.186	75.4	9514	0.11–0.85
9	54,600	0.15	Discrete, in log layer	2.2	1.172	75.4	9514	0.09–0.97
10	67,500	0.05	Discrete, near wall also	1.6	0.906	128	7527	0.05–0.59
11	67,500	0.1	Discrete, near wall also	1.8	0.867	114	10,716	0.02–0.81
12	67,500	0.15	Discrete, near wall also	2.5	0.547	82	28,712	0–0.82

$We = (\rho(\frac{du}{dy})^2 D_b^2)/(\sigma/D_b)$ is defined as the ratio of shear at the bubble to the Laplace pressure inside the bubble, here $\mu \frac{du}{dy} = \tau_w = \rho u_\tau^2$. Froude number ($Fr = U/(gD_b(1 - (\rho_b/\rho_f)))^{0.5}$) is defined as the ratio of flow inertia to the bubble buoyancy, which is a measure of relative bubble rise. Froude and Weber number are not mentioned for smallest Re as the bubble is already layered on top wall in the visualization window

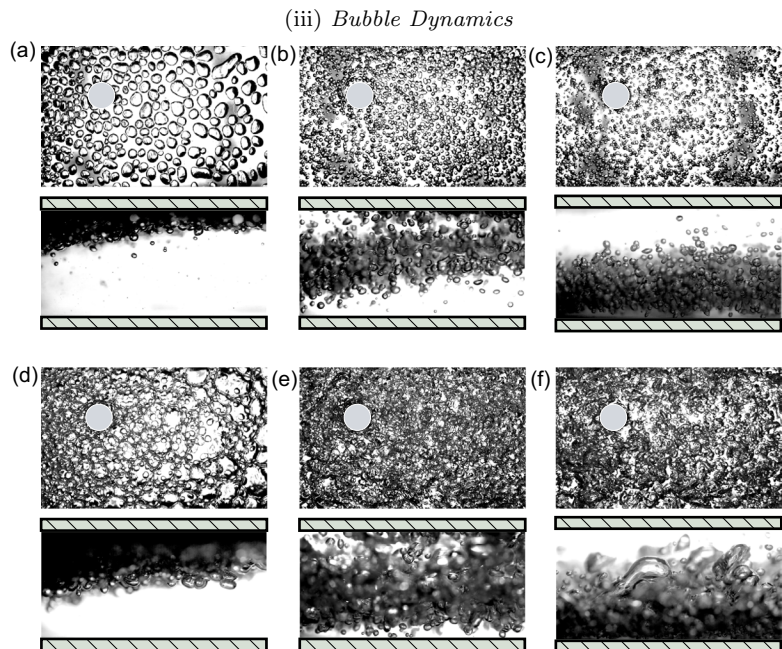
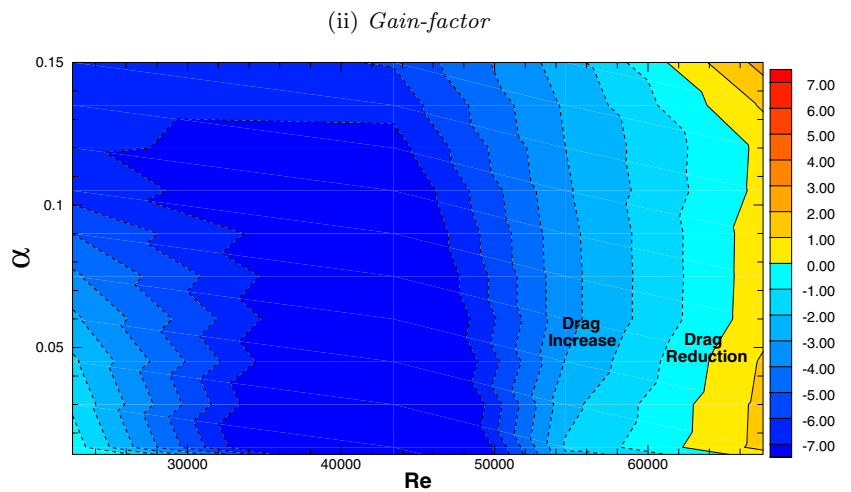
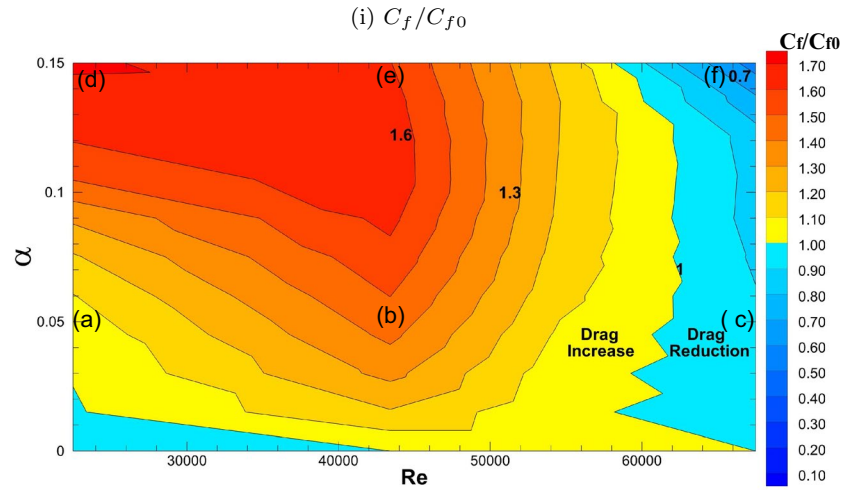
LWB: lower wall boundary layer

beyond which the bubble would break-up downstream. One important difference in the present work compared to some of the work from which Murai (2014) makes his inference is that the void fractions are considerably larger here. These larger void fractions in the present work bring into play the coalescence of bubbles, which leads to the larger observed bubble sizes and Weber numbers. It should be noted here that the process of break-up and the time-scales involved are larger than coalescence time-scales, and hence, bubble coalescence dominates over bubble break-up in the present work. The importance of the bubble We for drag reduction has been discussed by Van Gils et al. (2013), who show that bubble deformability seen at larger We is crucial for drag reduction. Broadly consistent with these observations, in the present experiments, within our set of data shown in Table 1, it is clear that higher drag reduction (lower C_f/C_{f0}) is achieved at larger values of We . Another important non-dimensional number in such flows is the Froude number, which is the ratio of flow inertia to buoyancy, and is defined here as $Fr = U/(gD_b(1 - (\rho_b/\rho_f)))^{0.5}$. Larger values of Fr (or Re) would imply lower bubble rise velocities, which would keep bubble within the bottom-wall boundary layer longer, and thus help with reduction of the bottom-wall shear. This is evident from the table, with larger Fr cases also corresponding to larger Re cases showing relatively lower values of C_f/C_{f0} (or higher drag reduction).

From Fig. 7(i), we can see that at Re of 22,500, drag increase is observed for all non-zero α values, with the corresponding gain values (in Fig. 7b) being negative, consistent with the increased pressure drop values in Fig. 5a. At this Re , if we look at bubble dynamics for α of 0.05, as shown in Fig. 7(iii)c, we observe that there are flat bubbles

near the top wall. These bubbles have migrated to the top wall after injection at the bottom wall due to buoyancy, with almost all bubbles reaching the top wall after traversing the vertical height of the channel. We should remember that the bubbles are injected 100 mm upstream of the visualization window. As discussed earlier, at lower Re , the vertical migration of bubbles is faster than at higher Re , and this is clear in this low Re case where the large bubbles that detach from the bottom wall travel all the way up to the top wall over a relatively short downstream distance. Given this fact, the broad bubble dynamics regime (BDR) is these cases, as given in Table 1, is either large coalesced bubbles at the top wall or air layer at the top wall. In these cases, where large bubbles are at the top wall for significant downstream distances and not in the bulk, the We and Fr values are not meaningful and, hence, have not been shown in Table 1. In these cases, a closer look at the corresponding pressure drop plot (Fig. 5a) shows that the pressure drop is higher at the top wall, compared to the lower wall. This is likely due to the fact that the bubbles reach the top wall after disturbing the top-wall boundary layer. With increasing α at this Re of 22,500, we observe bigger bubble sizes and a corresponding increase in wall drag (C_f/C_{f0}) to about 60% of the base case value. At higher Re of 43,400 in Fig. 5b, we again observe an increase in pressure drop compared to the base case, but the relative increase is smaller than at the Re of 22,500. For this case, all the bubbles have not reached near the top wall (Fig. 7b) as the flow velocity is larger here, and the time available for migration is smaller. With further increase in Re to 54,600 (Fig. 5c), we observe a small reduction in pressure drop at the bottom wall, whereas at other heights, we

Fig. 7 Plot shows the contour of C_f/C_{f0} for bottom-wall injection in the $Re-\alpha$ plane. In most of the $Re-\alpha$ plane, the bubbles in this case lead to drag increase. Drag reduction is only seen at the largest Re cases and is found to increase with α . Bubble visualizations at six conditions marked on the contour plot as **a-f** are also shown



still find an increase in pressure drop, with the overall integrated drag being larger than the base case. Corresponding to this increase in pressure drop and drag, the gain plot is negative over this range of Re and α . In all these Re cases, drag increases with α , with the largest drag corresponding to small Re and large α , where all bubbles reach the top wall after disturbing the top-wall boundary layer. We should note that in all these bottom-wall injection cases, the drag values shown correspond to the average drag over a stream-wise length of $12H$ (12 channel heights), and should be interpreted as the average of the different bubble interactions that take place over this length.

At even higher Re of 67,500, we observe a large reduction in pressure drop at the bottom wall (Fig. 5d). Most of the bubbles in this case are in the bottom-wall boundary layer (Fig. 7c), but we interestingly also observe a small reduction in pressure drop at the top wall. This is probably linked to the fact that in channel flow, boundary layer/vorticity on top and bottom walls mutually affect each other, and hence, the pressure drop decreases at the top wall despite the absence of bubbles there. At this Re , a surprising result occurs for $\alpha \geq 0.12$ with the bottom-wall pressure drop becoming negative, i.e., the pressure rises along the flow direction close to the lower wall. As this result was surprising, we repeated these experiments many times to gain confidence in the measurements, and the results were repeatable. One possible reason for this surprising result may be due to the energy released during bubble coalescence, which would be added to the flow. We estimated the total interfacial (surface) energy released per unit time compared to the power loss by the drag. We estimated the interfacial (surface) energy release as a result of the bubble size of 200 μm (near injection) coalescing to the final (near measurement section) bubble size of 2.5 mm, as observed for Re of 67,500 and α of 0.15. The interfacial energy released in this case and the drag energy loss are both of similar magnitude. Thus, interfacial energy release could be a probable cause for the observed negative pressure drop in the channel.

Another possible reason may be related to the observed negative Reynolds stress close to the wall by Hara et al. (2011) and Murai et al. (2006), which they relate either to the bubble's relative motion to the liquid or bubble-induced lift-up of vortical structures from the wall. Negative Reynolds stress can feed energy to the mean flow from the fluctuating component causing suppression of turbulence and wall drag. In these previous studies, PIV and PTV have been done at low void fraction only, but in the present study, pressure has been measured till very high void fraction. As there is variation in pressure drop in the vertical direction, the mean flow streamline will also be curved. We should keep in mind that locally near the bottom wall, the pressure drop is negative, but in the integral sense, the overall wall drag is positive but lower than the base case (about 55% of base case

for $Re = 67,500$ and $\alpha = 0.16$). The contour plot of C_f/C_{f0} in Re - α plane shows that drag is reduced only for the Re of 67,500 case, and at this Re , drag reduction increases with α reaching about 50% drag reduction at the highest void fractions. The corresponding gain factor is small (1–2), indicating that the drag reduction per unit void fraction is not large in this case. This is broadly consistent with the observations of Murai (2014) for drag reduction by millimeter-sized bubbles injected from the bottom wall. We shall compare this in the next sub-section with gain values for the top-wall injection studies.

3.2 Top-wall injection

The top-wall bubble injection data are expected to be completely different from the bottom-wall injection data due to the fact that buoyancy would now keep the injected air close to the top surface. This may be seen from pressure drop (ΔP) measurements with vertical height (y) for different bubble void fraction (α) for top-wall injection shown in Fig. 8 corresponding to four different Re values, as shown earlier for the bottom-wall injection case. In contrast to the bottom-wall injection, we observe that there are only small vertical regions where the pressure drop is higher, while in large parts of the height, there is significant reduction in pressure drop values compared to the base case. We also present in Fig. 10, contour plot of the overall (C_f/C_{f0}) values and the gain factor, along with bubble visualization images at six different conditions Fig. 10a–f, as done in the previous section for the bottom-wall injection case. As observed in the pressure drop data, we can see that, in general, there is considerable drag reduction over a large part of the Re - α plane, with a relatively small region where there is a mild drag increase. It may be noted that with the establishment of a complete air layer, there would be a huge reduction in shear at the top wall, and one might expect it to behave almost like an open channel. However, as seen from the top-wall injection measurements (Fig. 10), 50% drag is observed only at low Reynolds number and high void fraction (case Fig. 10d), where a relatively calm and complete air layer is formed. In all other cases, the drag is considerably different, and is related to the different bubble dynamics observed, which includes discrete bubbles at the top wall and the presence of void waves.

As expected, and as is clear from the side-view images, the injected air from the top wall remains close to the top wall in these cases due to buoyancy, and hence, the flow is not spatially developing in this case. An important measure in these cases is the vertical extent or thickness of the bubble/air layer formed on the top wall. It should be noted that we use the term bubble/air layer thickness, as the air at the top wall is in some cases in the form of discrete bubbles, while in other cases, it is in the form of a contiguous air

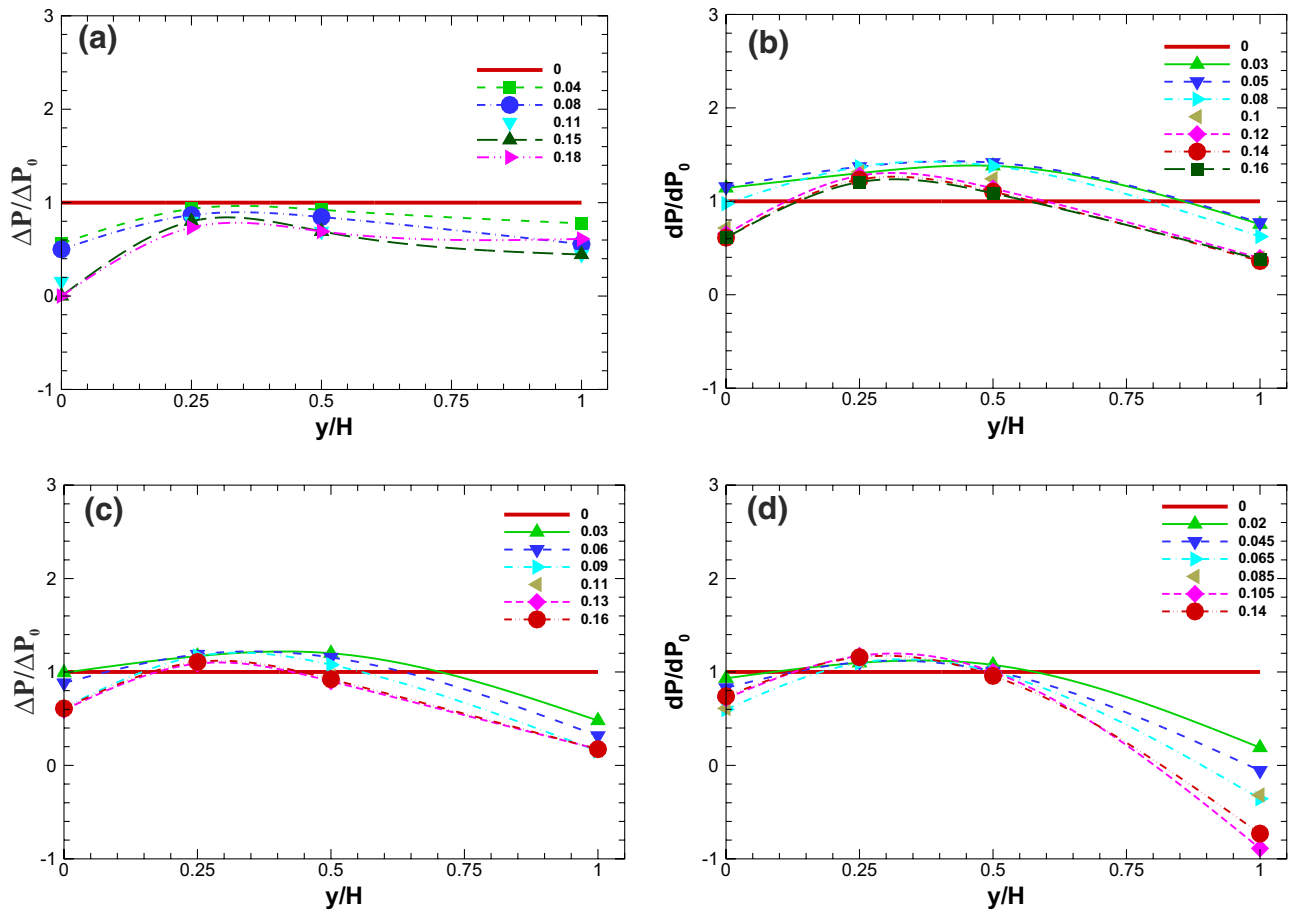


Fig. 8 Vertical variation of pressure drop non-dimensionalised by the base case pressure drop ($\Delta P/\Delta P_0$), for different void fraction (α) for top-wall injection. The flow Re corresponding to each of the plot is **a** 22,500, **b** 43,400, **c** 54,600, and **d** 67,500, respectively

layer. The vertical extent of the bubble/air layer (a_t/H) may be obtained from intensity profiles of the side-view visualizations after averaging a large number of instantaneous side-view images, with a cut-off for defining the thickness being at 50% of the value between the full-bubble intensity and the no-bubble intensity. In Fig. 9, we show the variation of bubble/air layer thickness (a_t/H) for different Re and α cases investigated here. At low values of $\alpha = 0.05$, corresponding to discrete bubbles on the top wall, (a_t/H) represents the average vertical extent or thickness of the bubble layer formed at the top wall. As α is increased from 0.05 to 0.1, at any given Re , there is a large increase in (a_t/H). This is related to the transition from discrete bubbles to a continuous air layer being formed at the top wall, with the air layer in general also having a region below it with fine discrete bubbles, as seen in the present side-view images. As discussed by Elbing et al. (2013) in the context of high Reynolds number flat plate boundary layer, an air layer forms once a critical air-flow rate is reached, with the existence of smaller discrete bubbles below the air layer as indicated by the lower void fraction region below the air layer.

In the present context of a channel flow, a complete air layer is formed for $\alpha \approx 0.1$ in most cases. Once the complete air layer is formed there is a large increase in the visual bubble/air layer thickness as measured here compared to the lower $\alpha = 0.05$ case. In the present context, such smaller discrete bubbles would increase the effective size of the bubble layer as seen from the side-view. Furthermore, increase in α from 0.05 to 0.1, however, appears to lead to a very marginal increase in the measured air/bubble layer; this perhaps being a reflection of the fact that the additional air is just occupying the relatively sparse region below the air layer, without affecting the overall measured bubble/air layer thickness. A summary of the measured bubble/air layer thickness on the top wall for different Re and α conditions investigated is shown in Table 2 along with broad bubble dynamics regime (BDR) and measured drag. More discussion and connections between the visualized bubble dynamics, the vertical pressure distribution, and the modified drag for the different conditions are given below.

At low $Re = 22,500$ and $\alpha = 0.05$, corresponding to condition Fig. 10a, we can see flat bubbles near the top, while at

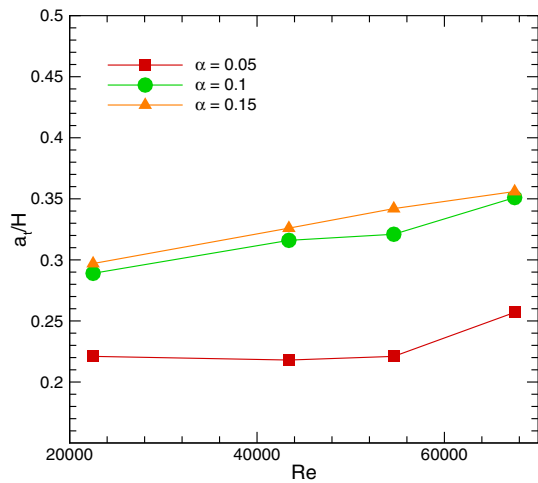


Fig. 9 Plot shows the air/bubble layer thickness (a_t/H) for top-wall injection. The data are obtained from averaging of side-view bubble visualizations. The values of a_t/H are seen to increase rapidly with α from 0.05 to 0.1, and thereafter, the increase with α is very small once the complete air layer is formed. At higher α values, significant increase in a_t/H is observed with Re , corresponding to the regime where we observe bubble void waves and thus dynamics may be more complex

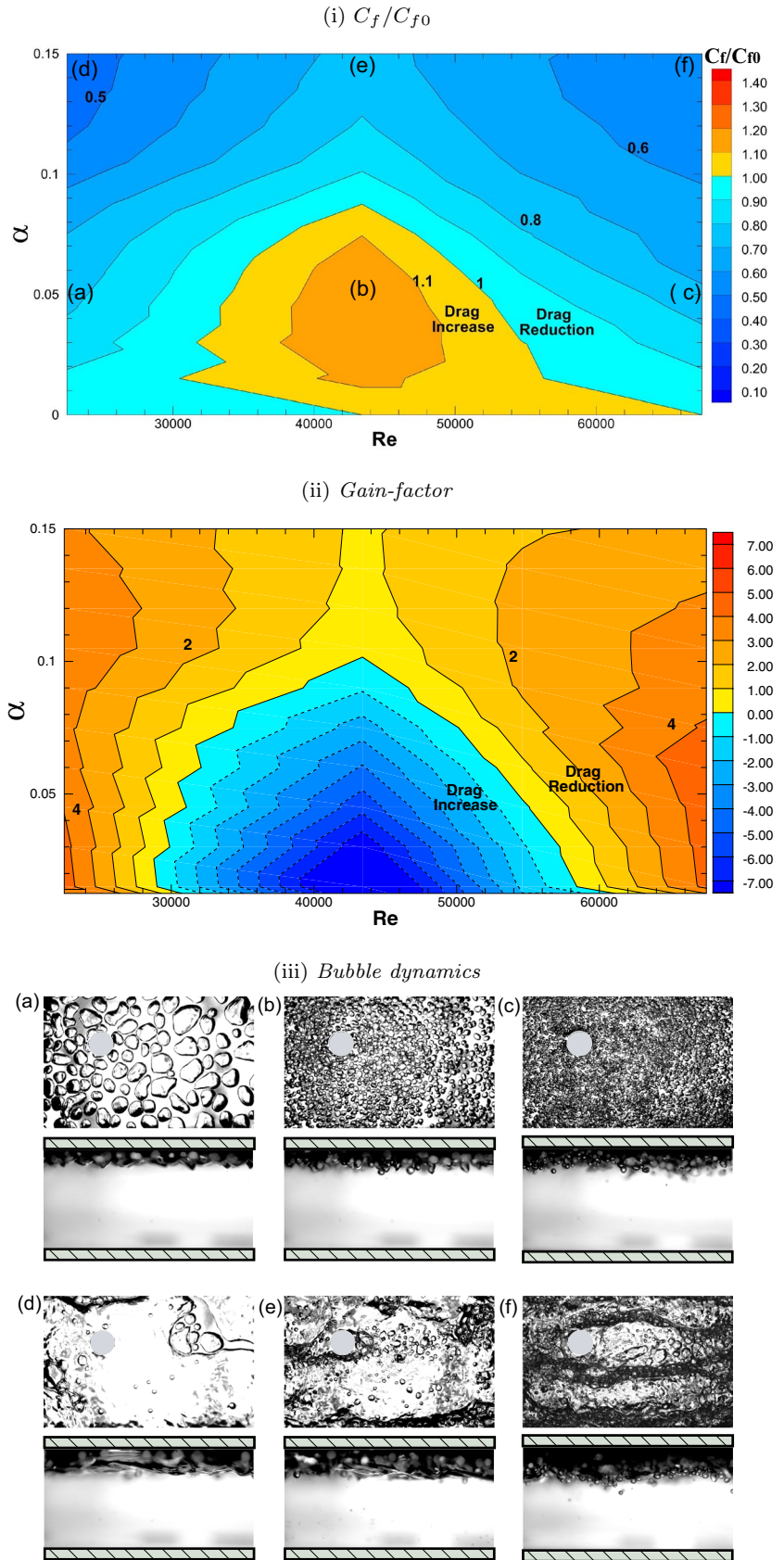
higher $\alpha = 0.15$ (condition Fig. 10d), we see an intermittent large air layer at the wall in Fig. 10(iii); both these bubble dynamics help to reduce the drag by changing conditions at and near the wall. The drag reduction is naturally higher for the nearly continuous air layer in Fig. 10d, compared to the flat bubble case in Fig. 10a. In general, as α is increased from small values, one might expect an increase of the fraction of the top wall covered by flat bubbles to increase, until a continuous air layer is formed, with a concomitant reduction in wall drag followed by a saturation of drag reduction, as observed by Elbing et al. (2013) in zero-pressure gradient turbulent boundary layer. We observe a maximum drag reduction of about 55% at this Re . For the flow Re of

43,400 and α of 0.05 (Fig. 10(iii)b), there are discrete bubbles near the top wall, which does not help in drag reduction. These are found to actually enhance the drag slightly (about 10%) as seen in the contour plot. Bubble size for this case is about 4.3 mm and it does not seem to be layered on the top wall from the bubble visualization images. We have previously seen that critical bubble diameter for shedding is about 1.5 mm, and thus, the 4.3 mm bubble would be expected to have shedding, which can explain the observed drag increase. With increasing α values, the air layer forms (condition Fig. 10e) and this again leads to drag reduction. At higher Re of 67,500, we observe small discrete bubbles at low α , which give mild drag reduction. As the void fraction is increased at this Re , the air layer forms with bubble waves, as may be seen in Fig. 10f, and this is found to lead to large drag reduction of about 45%. This kind of clustering for light particles and bubbles in turbulent flow is also discussed by Tagawa et al. (2012), and they show that it is mainly due to clustering in high vorticity region and bubbles remain clustered for much longer times than the flow structures which cause the clustering. These bubble/void waves will cause fluctuations in pressure as discussed in detail by Park et al. (2016, 2018). However, in the present studies, we have only concentrated on average pressure drop. For Re of 67,500 and high void fraction, we again observe more than 100% pressure drop reduction locally at the top wall from where bubbles are injected (Fig. 8d), similar to the bottom wall at same Re and about same α . We estimated the total interfacial (surface) energy released per unit time compared to the power loss by the drag. We estimated the interfacial (surface) energy release as a result of the bubble size of 200 μm (near injection) coalescing to the final (near measurement section) bubble size of 2.5 mm, as observed for Re of 67,500 and α of 0.15. The interfacial energy released in this case and the drag energy loss are both of similar magnitude. Thus, interfacial energy release could be a probable cause for the observed negative pressure drop in the channel. At

Table 2 Experimental conditions, bubble dynamics regimes, bubble size, drag reduction, and bubble/air layer thickness (a_t) for top-wall injection are summarized

Case	Re	α	Bubble dynamics regime	D_b (mm)	C_f/C_{f0}	a_t/H
1	22,500	0.05	Coalesced bubbles	7.7	0.771	0.221
2	22,500	0.1	Layering	37.7	0.56	0.289
3	22,500	0.15	Layering	84.5	0.44	0.297
4	43,400	0.05	Coalesced bubbles	4.33	1.189	0.218
5	43,400	0.1	Layering	29.5	0.907	0.316
6	43,400	0.15	Layering	90.2	0.742	0.326
7	54,600	0.05	Discrete	3.3	0.94	0.221
8	54,600	0.1	Coalesced bubbles	21.9	0.701	0.321
9	54,600	0.15	Bubble waves along side air layer	116.8	0.61	0.342
10	67,500	0.05	Discrete	2.65	0.728	0.257
11	67,500	0.1	Start of layer and bubble waves	42.6	0.583	0.351
12	67,500	0.15	Bubble waves along side air layer	118.4	0.56	0.356

Fig. 10 Plot shows the contour of C_f/C_{f0} for the top-wall injection in the $Re-\alpha$ plane. In most of the $Re-\alpha$ plane; the bubbles in this case induce drag reduction. Bubble visualizations at six conditions marked on the contour plot as **a-f** are also shown



Re of 67,500, we again observe saturation of drag reduction with increasing α , as shown in Fig. 10, and maximum drag reduction of about 45% is observed. One can see here for the top-wall injection case that the drag reduction saturates at higher void fractions in each Re case. It can be observed from the gain factor contour in the Re - α plane that a higher gain of about 4 is obtained at low and high Re and at low-to-moderate α , corresponding to bubble dynamics, as shown in Fig. 10a, c. This is significantly larger than the corresponding gain values for the bottom-wall injection cases seen in the previous section.

4 Conclusion

We have experimentally investigated within a single turbulent channel facility, drag modification using bubbles over a wide range of bubble void fraction ($0 < \alpha < 0.15$), channel Reynolds number ($22,500 < Re < 67,500$), and orientation of bubble injection (top/ bottom walls). In each of these cases, we have simultaneously measured drag modification and visualized the bubble dynamics in two perpendicular views. The modified drag is obtained from measurement of the mean pressure drop within the channel at four different vertical locations.

The results show that even in the same facility, the drag reduction obtained at a fixed void fraction (α) can be very different due to changes in bubble dynamics caused by changes in the other flow parameters. The visualizations show a number of bubble dynamics regimes depending on the parameters, with possibilities of both increased and decreased drag compared to the base case. The measurements for the bubble cases show significant vertical variations in the measured pressure drop within the channel, with these vertical variations being also dependent on the bubble distribution/dynamics. Interestingly, in some cases, the pressure drop at a given height even becomes negative, although the integrated pressure drop over the channel height, which is related to the overall drag, remains positive but lower than the base case. One possible reason for this surprising result may be the energy released during bubble coalescence, which would be added to the flow as the power release in coalescence is of similar magnitude to the drag power loss.

The measured drag data for the bubbly turbulent channel flow are presented as contours in the plane of Re and α , with a separate one for bottom- and top-wall injection cases, respectively. These contours of drag are very organized in contrast to the scatter seen when the drag data are plotted only with α . The variations in drag within these contours plots are gradual, and are, as expected, well correlated with the different types of bubble dynamics seen in the channel from the visualizations.

In terms of the overall drag, the bottom-wall injection cases show an increased drag over most of the range of Re and α investigated, with drag reduction seen only at the largest Re studied. In this case, apart from the nature of the bubble dynamics, the vertical migration of the bubbles away from the bottom wall plays a crucial part in deciding the drag. The measurements for this case show that at low Re , drag continually increases with α , while at high Re , the drag continually decreases with α . The maximum drag reduction observed is about 50% in this case, while drag increase of up to 60% has also been seen. On the other hand, the top-wall injection case shows drag reductions over a large part of the Re - α plane investigated, with the drag reduction in general increasing with α until a saturation value of drag reduction is reached corresponding in general to the formation of a continuous air layer at the top wall with some differences depending on the Re . In this case, the maximum drag reduction is considerably larger with up to 60% reduction in wall drag being observed.

In summary, the present measurements of drag modification and bubble dynamics over a large range of Re and α in a single turbulent channel help to delineate the different regimes seen in such bubbly channel flows.

Acknowledgements We are thankful to Prof. O. N. Ramesh, Anil Das, Akhilesh Prabhu, and Navneet Kumar for fruitful discussions and critical comments. We are also grateful to Subhajit Biswas and Naresh Kumar S. for all their help with the experiments. The third author acknowledges support from the Science and Engineering Research Board (SERB), India (SERB/F/5465/2018-2019). PBC Fellowship at Weizmann institute for NKJ is gratefully acknowledged.


References

- Ceccio SL (2010) Friction drag reduction of external flows with bubble and gas injection. *Annu Rev Fluid Mech* 42:183–203
- Coles D (1956) The law of the wake in the turbulent boundary layer. *J Fluid Mech* 1(2):191–226
- Dean R (1978) Reynolds number dependence of skin friction and other bulk flow variables in two-dimensional rectangular duct flow. *J Fluids Eng* 100(2):215–223
- Elbing BR, Winkel ES, Lay KA, Ceccio SL, Dowling DR, Perlin M (2008) Bubble-induced skin-friction drag reduction and the abrupt transition to air-layer drag reduction. *J Fluid Mech* 612:201–236
- Elbing BR, Mäkiharju S, Wiggins A, Perlin M, Dowling DR, Ceccio SL (2013) On the scaling of air layer drag reduction. *J Fluid Mech* 717:484–513
- Ferrante A, Elghobashi S (2004) On the physical mechanisms of drag reduction in a spatially developing turbulent boundary layer laden with microbubbles. *J Fluid Mech* 503:345–355
- Gabillet C, Colin C, Fabre J (2002) Experimental study of bubble injection in a turbulent boundary layer. *Int J Multiph Flow* 28(4):553–578
- Guin MM, Kato H, Yamaguchi H, Maeda M, Miyayama M (1996) Reduction of skin friction by microbubbles and its relation with near-wall bubble concentration in a channel. *J Mar Sci Technol* 1(5):241–254

- Hara K, Suzuki T, Yamamoto F (2011) Image analysis applied to study on frictional-drag reduction by electrolytic microbubbles in a turbulent channel flow. *Exp Fluids* 50(3):715–727
- Jacob B, Olivieri A, Miozzi M, Campana EF, Piva R (2010) Drag reduction by microbubbles in a turbulent boundary layer. *Phys Fluids (1994–present)* 22(11):115,104
- Jha NK, Govardhan R (2015) Interaction of a vortex ring with a single bubble: bubble and vorticity dynamics. *J Fluid Mech* 773:460–497
- Kumagai I, Takahashi Y, Murai Y (2015) Power-saving device for air bubble generation using a hydrofoil to reduce ship drag: theory, experiments, and application to ships. *Ocean Eng* 95:183–194
- Latorre R, Miller A, Philips R (2003) Micro-bubble resistance reduction on a model ses catamaran. *Ocean Eng* 30(17):2297–2309
- Lo T, L'vov VS, Procaccia I (2006) Drag reduction by compressible bubbles. *Phys Rev E* 73(3):036,308
- Lu J, Fernández A, Tryggvason G (2005) The effect of bubbles on the wall drag in a turbulent channel flow. *Phys Fluids (1994–present)* 17(9):095,102
- L'vov VS, Pomyalov A, Procaccia I, Tiberkevich V (2005) Drag reduction by microbubbles in turbulent flows: the limit of minute bubbles. *Phys Rev Lett* 94(17):174,502
- Madavan N, Deutsch S, Merkle C (1985) Measurements of local skin friction in a microbubble-modified turbulent boundary layer. *J Fluid Mech* 156:237–256
- McCormick ME, Bhattacharyya R (1973) Drag reduction of a submersible hull by electrolysis. *Nav Eng J* 85(2):11–16
- Meng JC, Uhlman J (1998) Microbubble formation and splitting in a turbulent boundary layer for turbulence reduction. In: *Proceedings of the international symposium on seawater drag reduction*, vol 341355
- Mizokami S, Kawakita C, Kodan Y, Takano S, Higasa S, Shigenaga R (2010) Experimental study of air lubrication method and verification of effects on actual hull by means of sea trial. *Mitsubishi Heavy Ind Tech Rev* 47(3):41–47
- Monty JP (2005) *Developments in smooth wall turbulent duct flows*. PhD thesis, University of Melbourne, Department of Mechanical and Manufacturing Engineering
- Murai Y (2014) Frictional drag reduction by bubble injection. *Exp Fluids* 55(7):1–28
- Murai Y, Oishi Y, Takeda Y, Yamamoto F (2006) Turbulent shear stress profiles in a bubbly channel flow assessed by particle tracking velocimetry. *Exp Fluids* 41(2):343–352
- Oishi Y, Murai Y, Tasaka Y, Yasushi T (2009) Frictional drag reduction by wavy advection of deformable bubbles. In: *Journal of physics: conference series*, vol 147. IOP Publishing, p 012020
- Park HJ, Oishi Y, Tasaka Y, Murai Y (2016) Void waves propagating in the bubbly two-phase turbulent boundary layer beneath a flat-bottom model ship during drag reduction. *Exp Fluids* 57(12):178
- Park HJ, Tasaka Y, Murai Y (2018) Bubbly drag reduction accompanied by void wave generation inside turbulent boundary layers. *Exp Fluids* 59(11):166
- Pope SB (2000) *Turbulent flows*. Cambridge University Press, Cambridge
- Rothstein JP (2010) Slip on superhydrophobic surfaces. *Annu Rev Fluid Mech* 42:89–109
- Sanders WC, Winkel ES, Dowling DR, Perlin M, Ceccio SL (2006) Bubble friction drag reduction in a high-Reynolds-number flat-plate turbulent boundary layer. *J Fluid Mech* 552:353–380
- Sridhar G, Katz J (1999) Effect of entrained bubbles on the structure of vortex rings. *J Fluid Mech* 397(1):171–202
- Tagawa Y, Mercado JM, Prakash VN, Calzavarini E, Sun C, Lohse D (2012) Three-dimensional Lagrangian Voronoï analysis for clustering of particles and bubbles in turbulence. *J Fluid Mech* 693:201–215
- Van Gils DP, Narezo Guzman D, Sun C, Lohse D (2013) The importance of bubble deformability for strong drag reduction in bubbly turbulent Taylor–Couette flow. *J Fluid Mech* 722:317–347
- Verschoof RA, van der Veen RC, Sun C, Lohse D (2016) Bubble drag reduction requires large bubbles. *Phys Rev Lett* 117(10):104,502
- Wei T (1987) Reynolds number effects on the small scale structure of a turbulent channel flow. PhD thesis, University of Michigan
- White CM, Mungal MG (2008) Mechanics and prediction of turbulent drag reduction with polymer additives. *Annu Rev Fluid Mech* 40:235–256
- Zanoun ES, Durst F, Nagib H (2003) Evaluating the law of the wall in two-dimensional fully developed turbulent channel flows. *Phys Fluids (1994–present)* 15(10):3079–3089

Publisher's Note Springer Nature remains neutral with regard to jurisdictional claims in published maps and institutional affiliations.

Affiliations

Narsing K. Jha^{1,2} · Anubhav Bhatt^{1,3} · Raghuraman N. Govardhan¹ 

✉ Raghuraman N. Govardhan
rng@iisc.ac.in

¹ Department of Mechanical Engineering, Indian Institute of Science, Bangalore, India

² Present Address: Weizmann Institute of Science, Rehovot, Israel

³ Present Address: University of Michigan, Ann Arbor, USA